Martian clouds observed by Mars Global Surveyor Mars Orbiter Camera

Huiqun Wang and Andrew P. Ingersoll

Division of Geological and Planetary Sciences, California Institute of Technology, Pasadena, California, USA

Received 6 November 2001; revised 18 March 2002; accepted 22 April 2002; published 15 October 2002.

[1] We have made daily global maps that cover both polar and equatorial regions of Mars for L_s 135°–360° and 0°–111° using the Mars Global Surveyor (MGS) Mars Orbiter Camera (MOC) red and blue wide-angle swaths taken from May 1999 to January 2001. We study the seasonal distribution of condensate clouds and dust clouds during roughly 1 Martian year using these daily global maps. We present the development and decay of the tropical cloud belt and the polar hoods, the spatial and temporal distributions of lee waves and spiral clouds, and an unusual "aster" cloud above the volcanoes, consisting of rays around a central disk, like the flower. The tropical cloud belt contains mostly fibrous clouds during northern spring/early summer and convective clouds during middle/late northern summer. The detailed development and decay of the tropical cloud belt is nonuniform in longitude. Two distinct stormy periods in late summer precede the formation of the north and south circumpolar hoods. The north polar storms in late summer resemble baroclinic frontal systems on Earth but contain both dust and condensate clouds. Spiral clouds occur only in the northern high latitudes and only during northern spring and summer. The north polar hood displays a stationary wave number two structure during the fall and winter. The south polar hood has fewer streak clouds and lee wave clouds than the north polar hood. During this particular year the lee wave cloud abundance in the south had two peaks (in early fall and late winter), and the lee wave cloud abundance in the north had one peak (in early fall). *INDEX TERMS:* 0343 Atmospheric Composition and Structure: Planetary atmospheres (5405, 5407, 5409, 5704, 5705, 5707); 3346 Meteorology and Atmospheric Dynamics: Planetary meteorology (5445, 5739); 5409 Planetology: Solid Surface Planets: Atmospheres—structure and dynamics; 5445 Planetology: Solid Surface Planets: Meteorology (3346); *KEYWORDS:* Mars daily global map, Martian clouds, dust storm, spiral clouds, aster cloud

Citation: Wang, H., and A. P. Ingersoll, Martian clouds observed by Mars Global Surveyor Mars Orbiter Camera, *J. Geophys. Res.*, *107*(E10), 5078, doi:10.1029/2001JE001815, 2002.

1. Introduction

[2] The distribution of clouds is important for the understanding of the Martian atmosphere, and is closely related to the Martian water cycle, dust cycle, and CO_2 cycle. The polar hoods, tropical clouds and dust storms have long been known through telescopic and spacecraft observations [*Snyder and Moroz*, 1992; *Martin et al.*, 1992]. *French et al.* [1981] documented the distribution of fogs, dust plumes, streak clouds, cloud streets, wave clouds and lee waves using the Mariner 9 and some Viking Orbiter images. *Kahn* [1984] added the thin haze, moderate haze and thick haze categories, and constructed a more complete catalog by including all Mariner 9 and Viking images. He further discussed the meteorological implications. Viking Infrared Thermal Mapper (IRTM) data have also been used to map the distribution of water ice clouds [*Tamppari et al.*, 2000]. However, previous spacecraft observations have strong selection effects due to the characteristics of their orbits. For example, of the total of over 49,500 images taken by Viking, only 18 were taken north of 60°N during L_s 270° ~ 325° [*Kahn*, 1984].

[3] The Mars Global Surveyor (MGS) is in a polar orbit with a period of about two hours. The ascending leg of the orbit crosses the equator of Mars from south to north at about 1400 LT (2 PM local time). The red (575–625 nm) and blue (400–450 nm) "push broom" wide-angle cameras produce 7.5 km/pixel global map swaths. Twelve consecutive swaths can cover the whole planet in one day at this resolution. The operation of the Mars Orbiter Camera (MOC) is described by *Malin and Edgett* [2001]. The systematic spatial and temporal coverage of MGS provides us with a good opportunity to monitor clouds on Mars.

[4] Compared with other Martian imagery studies, the MOC has regular two-hour coverage in the red and blue wavelengths. Dust and condensate clouds can be simultaneously identified according to their different colors. The lifecycles of storms and the seasonal distribution of clouds can be easily monitored due to the systematic coverage. However, the observations are largely limited to the early afternoon hours.

0148-0227/02/2001JE001815$09.00

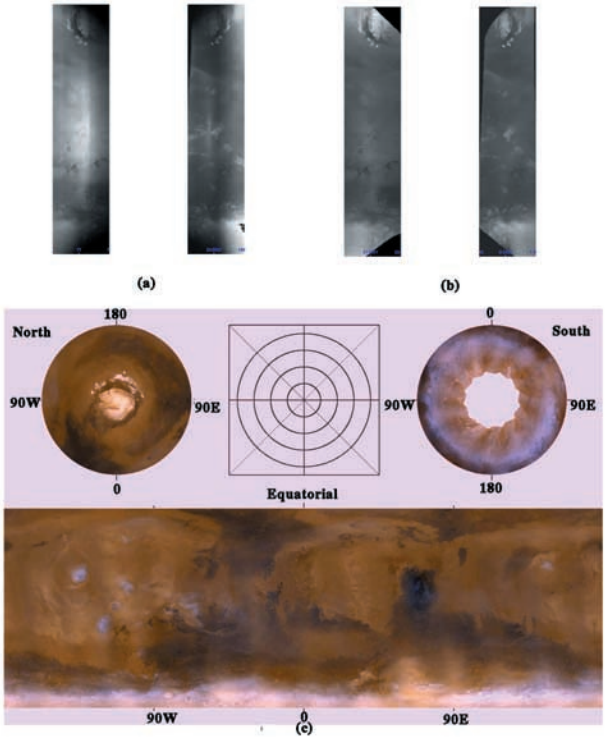

Figure 1. Image processing and daily global map. (a) Raw global map swath pair. Left: red image m02-01707. Right: blue image m02-01708. The blue image is flipped left-right with respect to the red image. (b) Processed global map swath pair. Left: red image m02-01707. Right: Blue image m0201708. (c) Daily global map for L_s ~154°. Upper left: north polar map (45°N–90°N, 0.1° × 0.1°) in polar stereographic projection. Upper right: south polar map (45°S–90°S, 0.1° × 0.1°) in polar stereographic projection. Lower: equatorial map (60°S–60°N, 0.1° × 0.1°) in simple cylindrical equidistant projection. The upper middle panel shows the pole and the latitudinal circles every 10° for the polar maps.

[5] We will show the global cloud distribution observed by MOC during the observational period of about one Martian year (May 1999 to January 2001: L_s 135°–360°–111°). Our data set is the same as that used by *Cantor et al.* [2001] in their comprehensive analysis of dust clouds. Our analysis covers both dust clouds and condensate clouds and the relationship between them. We will describe the development and decay of the tropical cloud belt and the polar hoods, the cloud morphology within the tropical cloud belt and the polar hoods, the evolution of streak clouds, the distribution of polar lee waves and spiral clouds, and the "aster" clouds associated with the volcanoes.

2. Data Processing

[6] A raw red and blue global map swath pair taken by MOC is shown in Figure 1a. The blue image is flipped left-right with respect to the red. The red image is more sensitive to dust clouds. The blue image is more sensitive to ice clouds [*James*, 1985; *Cantor et al.*, 2001]. Variable summation in the cross-track direction has been applied to these global images to maintain a fixed resolution of 7.5 km/pixel. The dark corners at the top and bottom are within the terminator (in darkness). The bright spot in the middle of each image occurs at 0°-phase angle. This brightness increase toward 0°-phase angle is called the "opposition surge" [*Hapke*, 1986]. It is a special case of the more general dependence of the observed brightness on the geometry that can be expressed as the bidirectional reflectance. Besides the geometry effect, variations in the camera response can also cause brightness variations in the global map swaths. Variations in the camera response have a low frequency component and a high frequency component [*Caplinger*, 1997]. The low frequency component refers to the general cross-track brightness variation in an image of an evenly bright target. The high frequency component refers to the pixel-to-pixel brightness variation (the vertical streaks in Figure 1a) due to the sensitivity variation of the camera CCD line array. The raw images are processed (see the next paragraph) so that these effects are minimized (see Figure 1b).

[7] To remove the low frequency brightness variations, including the opposition surge, we calculate the radiometric signal (data number/msec) generated at the focal plane using the MOC response equation in MOC2 calibration report [*Caplinger*, 1997]. We apply the following empirical function with parameters listed in Table 1 to both the red and the blue global map:

$$\begin{aligned} DN_{new} &= DN_{old}\,\frac{r(i_0,e_0,g_0)}{r(i,e,g)} \\ r(i,e,g) &= \frac{\mu_0}{\mu_0+\mu}H(\gamma,\mu_0)H(\gamma,\mu)\cdot \\ &\quad [f\cdot G(k_1,g)+(1-f)\cdot G(k_2,g)]\cdot \\ &\quad \left[1+\frac{B_0}{1+h_1\cdot\tan(g/2)}+\frac{a_1}{\exp(g/\alpha)}\right] \\ H(\gamma,x) &= \frac{1+2x}{1+2\gamma x} \\ G(k,g) &= \frac{1-k^2}{[1+k^2+2k\cdot\cos(g)]^{3/2}} \end{aligned} \tag{1}$$

where i is the incidence angle, e is the emission angle, g is the phase angle, $\mu_0 = \cos(i)$, $\mu = \cos(e)$. DN_{old} is the signal after just the gain and offset corrections, and DN_{new} is the signal after the photometric processing. γ is a parameter used to characterize the brightness dependence on incidence and emission angles, B_0 is the amplitude of the opposition surge, and h_1 is the half-width of the opposition surge [*Hapke*, 1986]. a_1 and α are additional parameters used to tune the shape of the opposition surge. k is the parameter used in the Henyey-Greenstein phase function $G(k, g)$. f is the fraction parameter.

[8] Equation (1) is similar to Hapke's bidirectional reflectance function [*Hapke*, 1986]. In order to derive the values for the parameters in Equation 1, we first selected red and blue images with small albedo variations from the early northern fall global map swaths that were available at the

Table 1. Parameters Used in Function (1) for Red and Blue Cameras

Filter	γ	B_0	h_1	a_1	α, °	f	k_1	k_2
Red	−0.0888	0.515	15.5	0.1	15.0	0.48	0.484	−0.112
Blue	0.615	1.05	17.5	0.8	20.0	0.92	0.82	−0.075

time when we developed the photometric calibration. In each image, the emission angle ranges from 0° to 90°, and the incidence angle ranges from ~20° to 90°. The phase angle ranges from 0° to 115°. These ranges are sufficient to determine the eight parameters of our model by the method of least squares. We attach no physical significance to the parameter values. Indeed, these parameter values include contributions from the low frequency response of the MOC as well as the Mars bidirectional reflectance. We use the model only to reduce the effects of viewing geometry and enhance the visibility of the clouds. The fit deteriorates toward the terminator, so the pixels with incident angles greater than ~87° are ignored in our processed images. Experiments with the global map swaths for this study show that in most cases, the opposition surges can be successfully removed, the clouds can be easily distinguished from the surfaces, and the seams between the overlap images in the daily global maps are much less apparent than the clouds and surfaces (see Figure 1c).

[9] To remove the high frequency brightness variations ("streaks," see Figure 1a), we use images in which the low frequency variations have been removed according to the above prescription. We determine the average brightness of each pixel in the MOC line array for low contrast scenes. The mean of this line array is normalized to unity and stored in a file. To process an image, we divide each line by this normalized line array. Figure 1b shows the processed images with the large-scale brightness variations and the streaks removed.

[10] We mosaic 13 consecutive global map swath pairs into a red and a blue daily global map. Consecutive maps overlap each other by one swath pair. We use a weighted average to mosaic the global map swaths, i.e., the pixel that has smaller incidence and phase angles and lies farther from the image corners makes a larger contribution to the value in the overlap region, and vice versa. Our currently processed global map swaths cover the period from L_s ~134° of the first Martian year to L_s ~111° of the second Martian year, where L_s is the areocentric longitude of the sun (Northern summer starts at L_s = 90°, and northern winter starts at L_s = 270°). All our daily global maps have the same 0.1° × 0.1° map grid. The equatorial map is in simple cylindrical equidistant projection and spans 60°S–60°N. The polar maps are in polar stereographic projections and extend out to ±45°. If there are missing data in the raw images, then gaps will occur accordingly in the daily global maps. To make three-color daily global maps, we first normalize the average brightness in the relatively cloud-free region between 10°N and 40°N, 305°-360°W for the equatorial maps, and that in the region between ~57.5°N and ~60°N, 90°-180°W for the polar maps. The same linear stretch is applied to all the red maps and likewise for the blue maps. We synthesize the green maps by combining 1/3 red and 2/3 blue and then apply a common linear stretch. The color daily global map for L_s ~154° is shown in Figure 1c. The terminator circle in the south polar maps is approximately outlined by the 87°-incidence angle, and the abnormal color near the terminator is due to the behavior of the photometric function (equation 1) at large incidence and phase angles.

[11] The equatorial and polar maps were animated to show the day to day changes on Mars. Each processed red and blue swath pair was projected and combined into a color image following the same procedure. Since the consecutive projected images in the polar region have relatively large overlaps, they were animated to show changes on a two-hour timescale.

3. Tropical Cloud Distribution

[12] The most prominent seasonal cloud variations during the Martian year are the development and decay of the north and south polar hoods and the tropical cloud belt. Figure 2 is a summary of cloud occurrence frequency in L_s intervals ~15° wide. In constructing Figure 2, we select pixels that are more than 25% brighter in the blue filter than the mean brightness of the map. The 25% threshold is valid only for our image processing, and was chosen so that the polar cap and condensate clouds are well identified. In most cases, dust storms are below this threshold. We verify these identifications by visual inspection. To enhance the contrast, we set the selected pixels in each daily equatorial map to the maximum value and other pixels to the mean value of the map. We then average these results over a range of L_s to get the panels of Figure 2. If there are missing data in a daily equatorial map, we fill in the gap with the values of the corresponding pixels from the previous day's or the next day's map, or it is left blank if no data exist for 3 consecutive days.

3.1. General Features

[13] The tropical cloud belt develops during northern mid spring, peaks around northern summer solstice, and decays during mid northern summer. This evolution is shown in Figure 2. The belt of clouds quickly disintegrates during L_s 134°~149°. As a result, only the topographic clouds associated with the volcanoes and Valles Marineris are left in late northern summer. These clouds keep diminishing until they redevelop at the beginning of the northern spring. The cloud patch associated with Arsia Mons is the only one that remains throughout the year. The cloud belt begins to develop after L_s ~44° in the second Martian year. It becomes longitudinally continuous during L_s 57°~70° and remains so until the end of our observational period, L_s ~111°. The fact that the tropical cloud belt appears in the northern spring and summer but not in the southern spring and summer is probably a reflection of the lack of water vapor sources in the southern hemisphere.

[14] The main belt lies between ~10°S and ~20°N. It is widest around Valles Marineris, and only weakly developed around Arabia Terra. Clouds occur most frequently around the volcanoes, Valles Marineris, and Syrtis Major. The evolution of the cloud belt this Martian year generally agrees with that of the Viking era water ice clouds [*Tamppari et al.*, 2000]. The differences occur mainly in northern spring around L_s ~65°. Compared with the MGS observations, the Viking era water ice clouds are more extensive near the upland regions including Arabia Terra, and the clouds near Valles Marineris appear poorly developed, compared with those in other longitudes.

3.2. Nonuniform Decay of the Tropical Cloud Belt

[15] The decaying phase of the tropical cloud belt in mid northern summer is short but complex. The cloud belt fluctuates on a timescales of days. Gaps appear at different

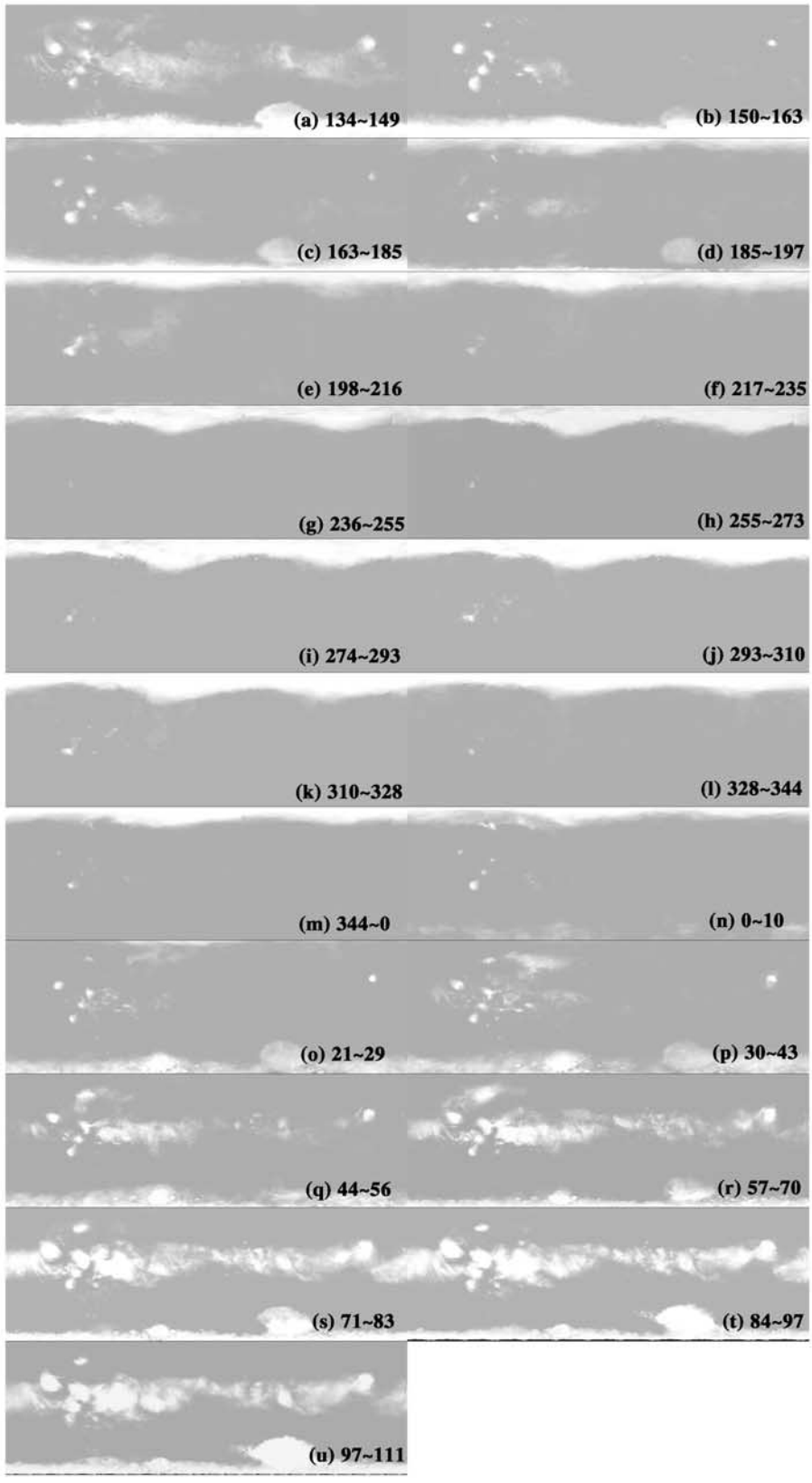

Figure 2. Seasonal cloud distribution in the equatorial maps. Each panel has the same format as the equatorial map shown in Figure 1. The panels are averages for the accompanying L_s intervals. See text for further detail.

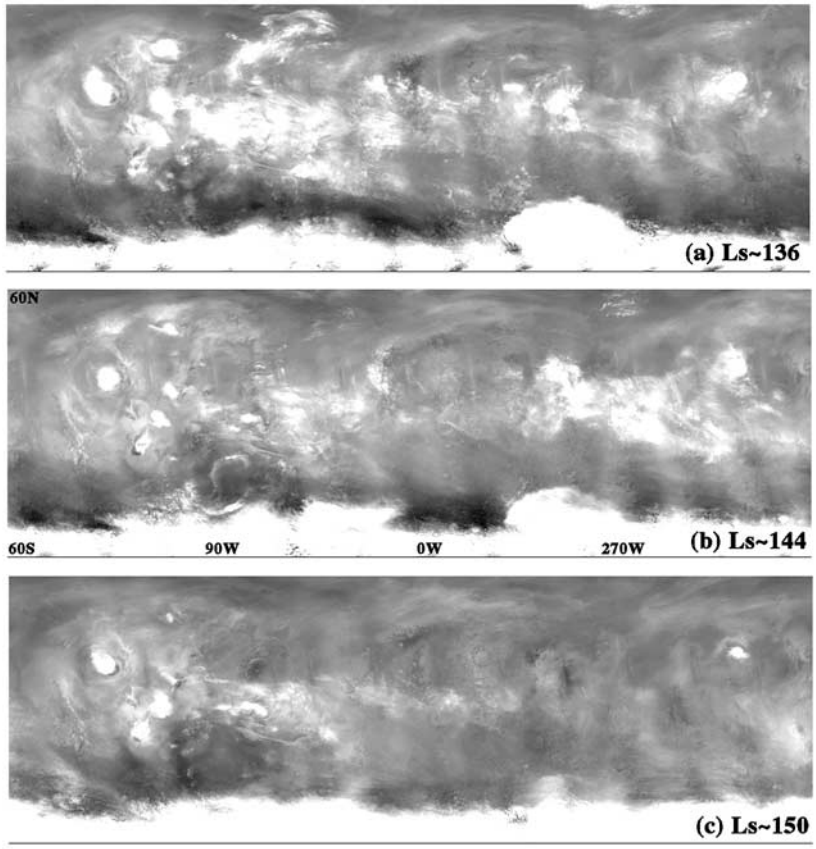

Figure 3. The decaying tropical cloud belt in mid northern summer. The panels have the same format as the equatorial map shown in Figure 1. Each panel is the blue filter map for a particular day at the L_s indicated in the figure.

longitudes, and the branches that extend off to higher latitudes fade away at different rates. These changes are shown in Figures 3a–3c). These are daily maps in contrast to those of Figure 2, which are averages over ~15° of L_s. The main cloud belt is sinuous and begins to break apart in Amazonis and Arabia Planitia during L_s 134°~142°. Clouds outside the main belt can often be observed at higher latitudes over Acidalia Planitia (see ~55°N, 50°W in Figure 3a), Utopia Planitia (see ~57°N, 275°W in Figure 3a) and Thaumasia Fossae (see ~35°S, 100°W in Figure 3a). The clouds over Acidalia Planitia often appear to be connected with the main tropical cloud belt through a branch of clouds near Tempe Fossae. Sometimes, a faint cloud branch can also be observed extending from southeast Valles Marineris toward Hellas basin. The clouds over Thaumasia Fossae sometimes appear to form a cloud branch as well. However, the clouds over Utopia Planitia remain disconnected from the main belt during our observational period (Figure 3a). There could be a branch of clouds connecting the Utopia clouds with the main belt earlier in the season, but they may have dissipated by the time of our observation. Cloud branches extending from the main belt toward higher latitudes have been observed by Hubble Space Telescope around L_s ~63° [*James et al.*, 1996], and they are simulated by GCM [*Richardson et al.*, 2002]. The clouds in the western hemisphere (0°-90°-180°W) diminish after L_s ~142°. The clouds between Syrtis and Elysium brighten briefly and then quickly disintegrate within about a week.

[16] The developing phase of the cloud belt is nonuniform too. During the MGS year, clouds developed first near Valles Marineris and last near Arabia Planitia (see Figure 2). This is just the opposite of that found by *Tamppari et al.* [2000] for the Viking era.

3.3. Cloud Morphology of the Tropical Cloud Belt

[17] Clouds in the tropical cloud belt belong to two main cloud types. Most of the clouds observed during L_s 44°~ 111° appear fibrous (see Figure 4a) and are similar to cirrus clouds on Earth [*Houze*, 1993]. However, the fraction of fibrous clouds decreases quickly after *Ls* ~134°. Cloud patches composed of small puffy plumes (see Figure 4b) become dominant from mid to late northern summer. These clouds resemble cumulus clouds on Earth. They indicate atmospheric convection and relatively weak horizontal winds [*Houze*, 1993]. Convective clouds are not limited to the main tropical cloud belt; they can be found at high latitudes and even near the polar cap (see Figures 4c–4e). Many high latitude convective clouds appear to be related to the main tropical cloud belt through cloud branches (see section 3.2). Sometimes, the convective clouds organize into cloud streets with parallel rows (Figures 4c and 4e). Cloud streets on Earth usually occur in a convective boundary layer with vertical wind shear, and they could align either parallel or perpendic-

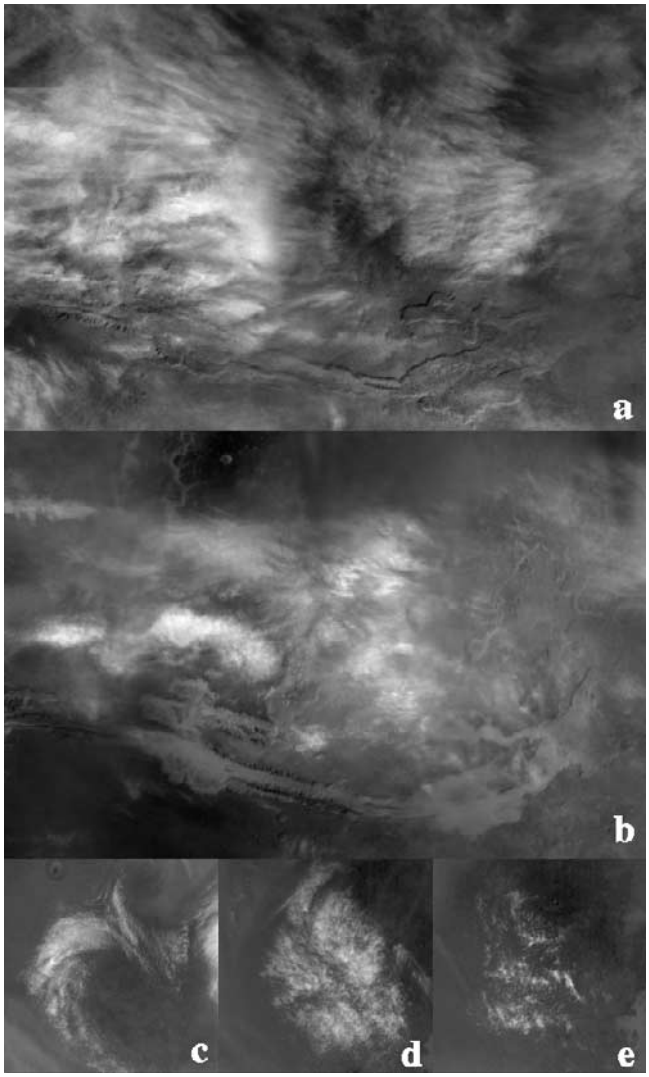

Figure 4. (a) Fibrous clouds north of Valles Marineris around L_s ~101.2°. (b) Convective clouds north of Valles Marineris around L_s ~149.8°. Both (a) and (b) are cropped from the corresponding blue equatorial maps (0.1° × 0.1°), and are composed of 600 × 400 pixels. (c) Cloud streets at ~53°N, 20°W around L_s ~134°. This 200 × 200 (pixel) image is cropped from global map swath m01-00017 (7.5 km/pixel). (d) Actinae clouds at ~56°N, 269°W around L_s ~139°. This 200 × 200 (pixel) image is cropped from global map swath m01-01949 (7.5 km/pixel). (e) Cloud streets at ~53°N, 264°W around L_s ~144°. This 200 × 200 (pixel) image is cropped from global map swath m01-03850 (7.5 km/pixel).

ular to the wind [*Houze*, 1993]. Sometimes, the convective clouds organize into radiating patterns (see Figure 4d) that are similar to ''actinae'' on Earth [*Houze*, 1993].

[18] In the Viking era, low latitude streak clouds (fibrous clouds) were observed more often during L_s 45° ~ 130°, while wave clouds and cloud streets (convective clouds) were mainly observed during L_s 80° ~ 130° [*Kahn*, 1984]. This indicates a change in cloud type in the tropical cloud belt and is consistent with the MOC observations. However, there are some differences. Convective clouds can still be observed in MOC images during L_s 134° ~ 150°, but few during the same period were observed in the Viking data [*Kahn*, 1984]. Low latitude streak clouds in the Viking era were also observed during L_s 245° ~ 360°, but few condensate clouds are observed in the MOC images during the same period of L_s.

[19] Large dust storms such as the mid northern fall cross-equatorial regional dust storms studied by *Cantor et al.* [2001] interact with the condensate clouds [*Smith et al.*, 2001; *Rodin et al.*, 1999]. Right after these regional dust storms, few condensate clouds are observed in the low latitudes (see Figure 2f). This negative correlation between the dust and condensate is in contrast with that during the formation of the north polar hood (see section 4). The disappearance of the condensate clouds here is perhaps because dust warms the atmosphere [*Smith et al.*, 2001] or dust particles serve as nucleation sites for ice removal [*Rodin et al.*, 1999]. However, the decrease of condensate clouds is imbedded in the general decline of the tropical cloud belt, so the role played by dust is unclear.

3.4. Aster Clouds Above the Volcanoes

[20] Topographic clouds associated with the volcanoes have been known for a long time through telescopic and spacecraft observations [*Martin et al.*, 1992; *Snyder and Moroz*, 1992], but only since MGS are daily synoptic observations possible. During mid to late northern summer, the clouds above the volcanoes sometimes take the form of rays around a central disk, like the flower. Some of the best examples are observed above Arsia Mons and are shown in Figure 5. Shadows cast by the ray clouds suggest that they are sometimes 15 km or more above the surface. The rays are usually 200–500 km long and 20–50 km wide. Clouds with similar morphology are also observed on other volcanoes, but are usually less regular in shape. Sometimes the central disk is missing, and sometimes the rays are parallel instead of radiating. The strong correlation of such clouds with the special topography of large volcanoes suggests that these clouds are related to the up-slope winds that are expected during daytime.

4. North Polar Clouds

[21] The north polar hood develops from a series of storms that first appear in late northern summer (Figure 6). By early northern fall, the polar region is covered by circumpolar clouds. The polar hood grows south of ~60°N after L_s ~185° and retreats north of ~60°N after L_s ~10° (see Figure 2). The north polar hood displays a stationary wave number two pattern (Figures 2e–2n). Clouds push further south in Acidalia Planitia (~30°W) and Utopia Planitia (~250°W) than in other longitudes, and they can reach latitudes as low as ~35°N. The north polar hood exhibited a wavy structure also during the Viking era [*French et al.*, 1981], as indicated by the lee waves and streak clouds. The wavy structure shows a strong correlation with topography and agrees well with the GCM simulated winter quasi-stationary eddies [*Barnes et al.*, 1996].

4.1. North Polar Hood Formation (L_s 160° ~ 185°)

[22] As the northern fall approaches, the north polar region enters a transitional period (L_s 160° ~ 185°) characterized by widespread condensate clouds and dust storms

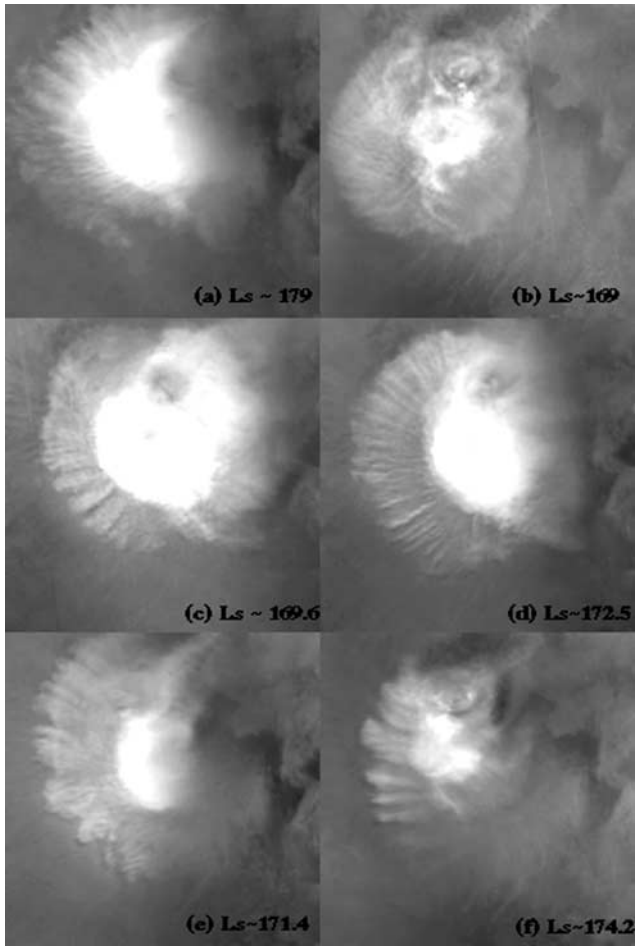

Figure 5. Aster clouds, consisting of rays around a central disk, above Arsia Mons (~9°S, 120°W) in mid northern summer. Each panel has 200 × 200 pixels and is cropped from the corresponding blue equatorial map (0.1° × 0.1°), simple cylindrical equidistant projection).

(Figures 6b and 6c). *Cantor et al.* [2001] documented the emergence of many local dust storms in late northern summer and the development of two regional dust storms that originated at L_s 163° and 183° respectively. The 270°–0°–90°W sector is especially active during L_s 160° ~ 185°. Many storms originate here and move eastward as they develop. These storms are associated with fronts. Many fronts form spiral clouds, which are discussed in section 4.4.

[23] The great increase in cloud cover during L_s 160° ~ 185° can be seen in Figure 7a, which shows the fraction of cloud-covered area between 60°N and 75°N as a function of L_s for three different criteria. (1) The green line represents pixels in the blue north polar map that are more than 75% brighter than the corresponding pixels in the reference blue map. This criterion selects both condensate and dust clouds (total clouds). (2) The blue line represents pixels in the blue north polar map that are 125% brighter than the reference blue map. This criterion selects thick condensate clouds. (3) The red line represents pixels in the red north polar map that are 25% brighter than the reference red map. This criterion selects thick dust clouds. The corresponding areas selected by these criteria are highlighted by the corresponding colors in Figures 7c–7e for the image shown in Figure 7b. The spiral dust storm in the image was studied by *Cantor et al.* [2001].

[24] The sharp increase in the total clouds (the green line in Figure 6) around L_s ~163° corresponds to the first regional dust storm described by *Cantor et al.* [2001]. By the time of the second regional storm (L_s ~183°), ~95% of the area between 60°N and 75°N was covered by clouds. Dust and condensate clouds that are especially thick will be selected both by criterion (2) and by criterion (3), so the sum of the red and blue areas is greater than the green area after L_s ~173°. Although the L_s ~163° regional storm induces an apparent increase in both the total clouds and the thick dust and condensate clouds (see Figure 7), the L_s ~183° storm is mainly associated with an increase in the thick clouds because the total cloud cover is already large before L_s ~183°. Between the L_s ~163° and 183° regional storms, the total clouds are significantly greater than the sum of the red and blue clouds, indicating the presence of haze, which does not register in criteria (2) and (3).

4.2. North Polar Streak Clouds

[25] The polar hood contains a wide range of cloud types: condensate and dust hazes, streak clouds, dust storms, clouds associated with frontal systems and lee waves (Figures 6c–6g). The presence of these clouds is consistent with the low atmospheric temperature, large temperature gradient between the mid and high latitudes, high near-surface static stability, strong wind speed and strong wind shear in the fall and winter [*Kahn*, 1984; *Haberle et al.*, 1993].

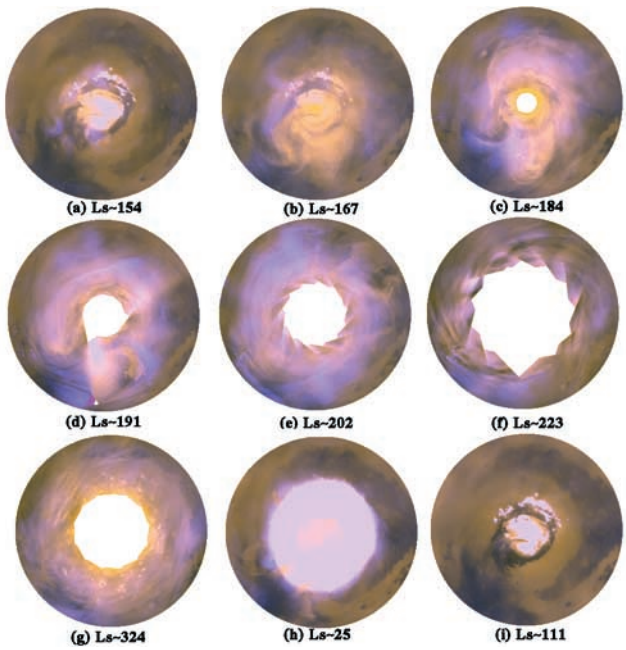

Figure 6. Representative north polar stereographic maps (45°N-90°N, 0.1° × 0.1°). The L_s is listed below each panel. The blank circular areas in the centers of the maps during the fall and winter are the areas inside the terminator circles, for which there are no data. The polar cap in Figure 6g is larger than that in Figure 6h, but it appears darker because the stretches are different. The abrupt change in brightness north of the triangular area in Figure 6d is related to missing data in one of the global map swaths.

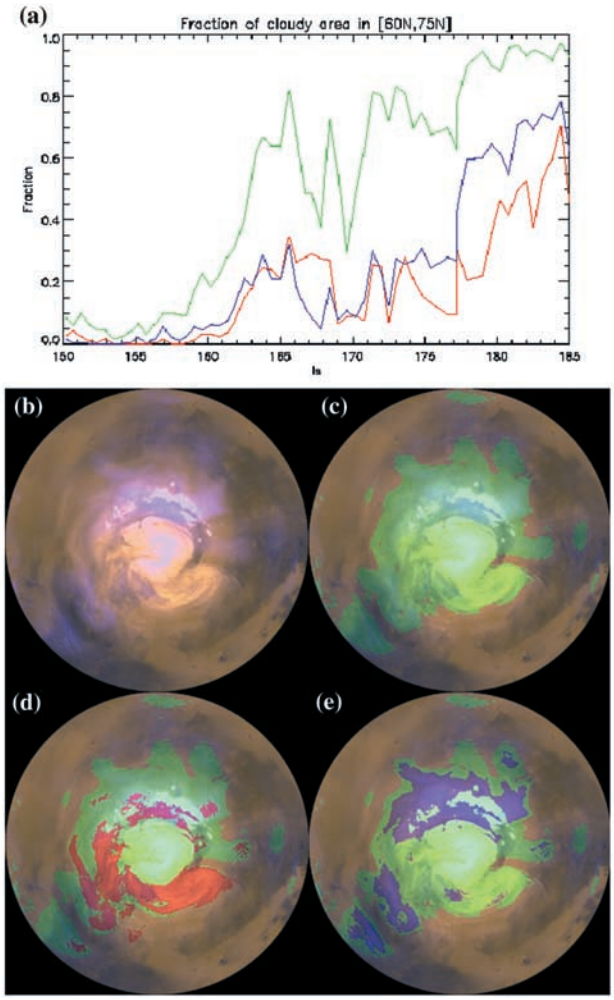

Figure 7. (a) The fraction of cloud covered area between 60°N and 75°N as a function of L_s for three different criteria used to identify clouds. (b) North polar stereographic map (45°N-90°N) at L_s ~164°. (c) The green area highlights the total clouds including both the dust and the condensate clouds. (d) The red area highlights dust clouds. (e) The blue highlights condensate clouds. See text for details.

[26] Streak clouds appear to be the most characteristic clouds in the polar hood. Streaks can occur in both condensate clouds and dust clouds [*Kahn*, 1984]. They usually appear as long curves that can be traced in several consecutive global map swaths for thousands of kilometers. The time interval between the consecutive swaths is about two hours. The fact that coherent streaks span several swaths suggests a lifetime of several hours. The streak clouds are usually associated with strong winds [*Kahn*, 1984]. Strong winds can advect particles great distances downwind and give a stringy appearance to the clouds [*Houze*, 1993]. The number of streaks in the north polar maps appear to increase from early to mid northern fall and decrease during the northern winter (see Figures 6d–6g), although the terminator circles near L_s ~270° obscure a large area. In comparison, *Kahn* [1984] observed significant decrease of streak clouds during the fall for the Viking era, but this could be related to the nonuniform image coverage at that time.

[27] The streaks observed in the north polar maps often appear to spiral counterclockwise in toward the pole, especially between mid northern fall and mid northern winter, and they seem to delineate a polar vortex that changes daily. Figures 8a–8f show the streaks traced in six consecutive north polar maps during L_s 202° ~ 205°. The arrows in the plot point in the wind directions indicated by the coexistent lee waves. Poleward converging counterclockwise streaks in the fall and winter are consistent with the low-level poleward meridional circulation in high latitudes simulated by GCM's [*Haberle et al.*, 1993]. The streaks usually dip to lower latitudes at Acidalia Planitia, Utopia Planitia or Arcadia Planitia. These areas have been simulated to be the wintertime storm zones on Mars [*Hollingsworth et al.*, 1996]. *Cantor et al.* [2001] describe three cross-equatorial regional dust storm events during mid northern fall (L_s 210° ~ 230°); another such storm is observed by MOC in mid northern winter (L_s ~320°). All these storms seem to originate from the northern storm zones and get entrained into the lower branch of the Hadley circulation through the western boundary jets [*Cantor et al.*, 2001]. Each regional dust storm appears to be composed of a series of storm centers that continuously push southward as they replenish dust to the atmosphere [*Cantor et al.*, 2001].

[28] As the amount of streak clouds decreases during the winter, the main clouds in the north polar hood change into haze and cap edge dust storms by L_s ~0°. The polar hood retreats with the polar cap to high latitudes. The recession of the north polar cap and the circumpolar dust activities are described by *James and Cantor* [2001]. Most of the areas outside the polar cap appear clear. Cap edge dust storms occur preferably in the 270°–0°–90°W sector during the spring and summer [*James and Cantor*, 2001]. Individual global map swaths often show cloud activity on the 0200 LT (2AM local time) side of the polar cap [*James and Cantor*, 2001]. These clouds do not show clearly in the daily north polar map because the 0200 LT side of one swath overlaps with the 1400 LT (2PM local time) side of another swath. More weight is assigned to the pixels on the 1400 LT side than those on the 0200 LT side when the swaths are merged to make daily north polar maps (see sections 2 and 5.2).

4.3. North Polar Lee Waves

[29] Lee waves are frequently observed in the polar region during fall and winter. They are associated with stationary gravity waves on the lee side of obstacles [*Kahn*, 1984]. On Earth, lee waves preferably occur in a layer with rapidly decreasing static stability and increasing wind speed with height [*Houze*, 1993]. The high near-surface static stability and strong wind shear during the fall and winter [*Haberle et al.*, 1993] could provide good conditions for Martian lee wave formation. The observed wavelengths of the lee waves range from ~15 km to ~50 km. Waves with shorter wavelengths cannot be recognized properly because they are not well resolved at 7.5 km/pixel. Lee waves usually appear superimposed on the haze and streak clouds. Examples can be seen near ~45°W, 50°N in Figures 6e and 6f.

[30] The spatial distribution of lee waves in the north polar maps (45°N–90°N) is shown in Figure 9a. More lee waves are observed between 45°N and 60°N than between 60°N and 90°N. This is largely because no MOC data exist within the terminator circles (see Figures 6e and 6f), which

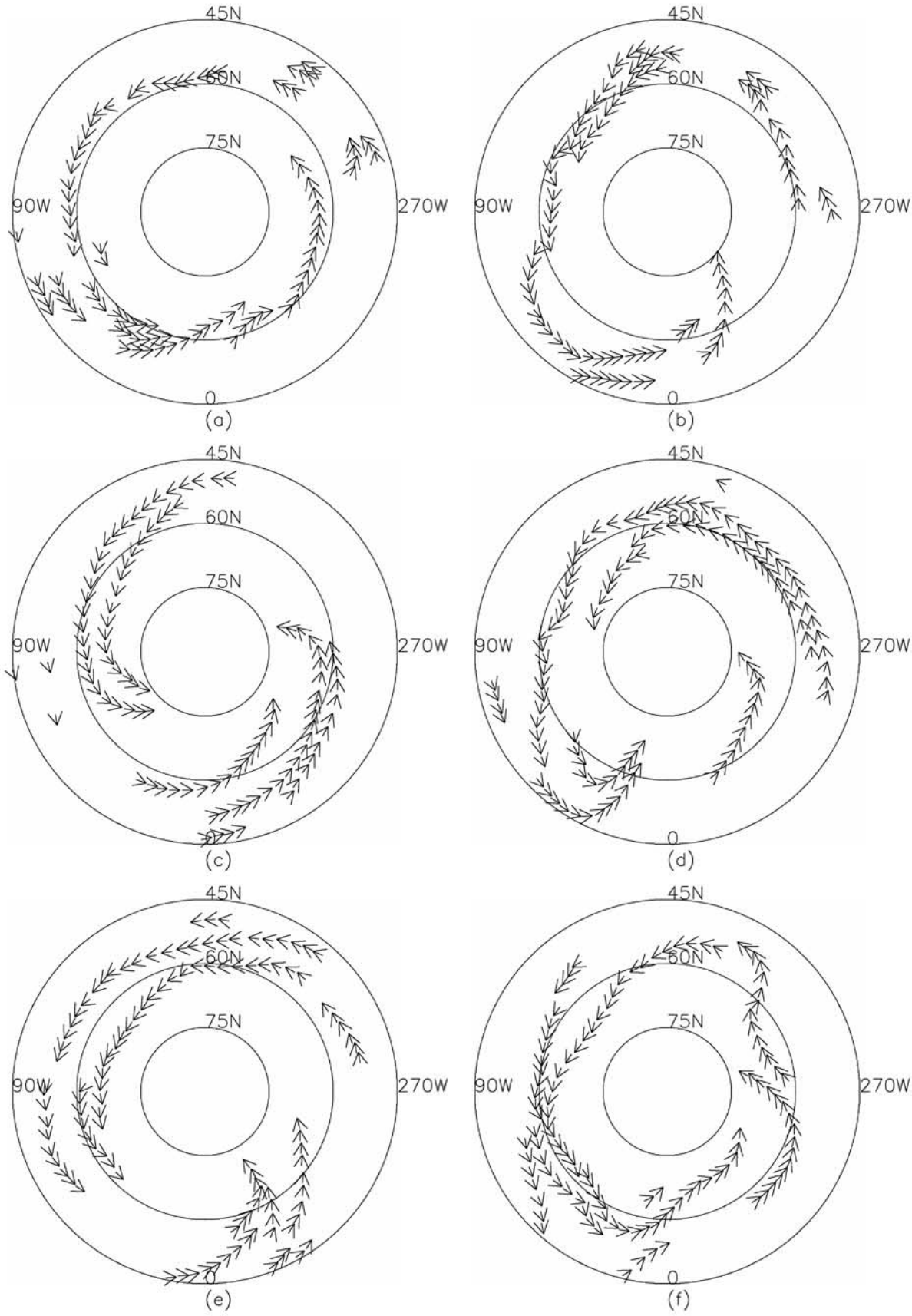

Figure 8. Streaks traced in six consecutive north polar maps (a–f) during L_s 202° ~ 205°. The arrows point in the wind direction indicated by the lee waves. The length of the arrow is arbitrary.

maximize at winter solstice. For comparison, MOLA observed many wave clouds with sloping fronts during the polar night within the terminator circles [*Pettengill and Ford*, 2000]. While lee waves seem widespread, many of them cluster around topographic features such as fossaes, mensaes and large craters. In late northern summer, lee waves suddenly increase in the 0°–90°–180°W hemisphere, then quickly spread to the opposite hemisphere (not shown).

[31] The number of lee waves observed in the north polar maps as a function of L_s is shown in Figure 10a. An eleven-day running mean has been applied to the original daily data to reduce high frequency variation (the solid line). To minimize the effect that no observations exist within the terminator circles which maximize at the winter solstice, the numbers represented by the solid line are then scaled by the area outside the terminator circles (the dotted line), so the number density is proportional to the dotted line. Lee waves sharply increase around L_s ~170°, peak around L_s ~195°, and quickly disappear after L_s ~20° of the second year. The decreasing trend from the early fall to the late winter is probably related to the decreasing amount of water vapor. Significant decrease of lee waves during the fall and winter was documented for the Viking era, although the high latitude coverage near the winter solstice was poor at that time [*Kahn*, 1984]. Several summertime north polar lee waves were observed in the Viking images [*Kahn*, 1984], but we observe no summertime lee waves in the MGS north polar maps. This may not necessarily reflect interannual variability, because most Viking images have resolution better than 1.5 km/pixel [*Snyder*, 1977], and the MOC global map swaths have a resolution of 7.5 km/pixel.

4.4. Spiral Clouds

[32] Viking spacecraft imaged a spiral cloud around 78°N, 150°W in early northern summer [*Hunt and James*, 1979; *Gierasch et al.*, 1979]. Hubble Space Telescope (HST) also observed such a cloud around 65°N, 85°W a few days before our observational period (NASA HST Press release NO. STSc1-PR99-22, May 19, 1999). These two pre-MGS spiral clouds were composed mainly of water ice and had cloud-free centers. However, the spiral clouds observed by MOC are mainly composed of dust, and many of them have associated spiral arms or fronts (see Figure 11). Some of them have associated condensate clouds during their developing phase (see Figure 12).

[33] All the spiral clouds observed during our observational period are summarized in Figure 11. Figures 11g and 11f were discussed by *Cantor et al.* [2001], and Figures 11k, 11m, and 11o were discussed by *James and Cantor* [2001]. All the spiral clouds observed by MGS occur in the northern high latitudes from mid northern spring to early northern fall (L_s 30° ~ 185°). The fact that no spiral clouds are observed in the south indicates different conditions of the two polar regions during the corresponding season (see section 5). The spiral cloud in Figure 11g lies in the 270°-360°W sector, and all the others lie in the 0°-90°W sector. This preference for the 0°-90°W sector may be related to the special local topography or thermal inertia. All of the 22 storms in Figure 11 spiral inward in the counterclockwise direction. Developing baroclinic disturbances on Earth have the same sense of rotation in the northern hemisphere. However, the center of the spiral ("comma-cloud" [*Houze*, 1993]) is usually to the north, where the cold front (on the western side) and warm font (on the eastern side) merge to form an occluded front. Some of the Martian storms have this property (e.g., Figure 11f). In other Martian storms, the center of the spiral is to the south and appears to belong to the putative cold front (e.g., Figures 12a–12c). The large temperature gradient between the polar cap and the circumpolar surface during the spring and summer [*Barnes et al.*, 1993; *James et al.*, 1999] is consistent with the occurrence of spiral clouds.

[34] The location of the condensate cloud in relation to the spiral dust clouds provides further support for the baroclinic disturbance hypothesis. Figure 12 shows two examples of cyclogenesis observed by MOC. Each leads to a regional spiral dust storm that is described in detail by *Cantor et al.* [2001]. The first row in Figure 12 shows three consecutive views (spanning 4 hours) of a storm around L_s ~163°. The spiral arm south of the cap sweeps eastward at ~20 m/s and approaches the dust front at ~315°W. Bluish condensate clouds can be seen just north of the dust front. Our interpretation is that the relatively warm, moist air south of the dust front is forced upward as it pushes northward over the colder polar air. Water vapor condenses above the condensation level and produces the observed condensate clouds. The dust front and the associated condensate cloud at ~315°W are analogous to a terrestrial warm front. The fast-moving spiral arm is analogous to a terrestrial cold front, but it has more curvature and a hook shape.

[35] The second row shows a storm around L_s ~182°. Two dust arms appear to be connected by a cyclonic spiral cloud to the north. The center of the spiral cloud moves eastward at ~15 m/s. The northern parts of the two dust arms appear to be colliding (Figures 12f and 12g). The southern tips of the two arms sweep eastward at ~20 m/s. Condensate clouds can be seen just east of the leading (eastern) dust arm in the 0°-45°W sector. This development process resembles the typical baroclinic storm genesis on the Earth [*Leovy et al.*, 1972], with the eastern arm being a warm front, the western arm a cold front, and the spiral cloud an occluded front.

[36] The spiral clouds from mid to late spring tend to occur right at the cap edge, and they sometimes have associated fronts that extend southward (Figure 11). The spiral clouds from early to mid summer usually lie south of the cap edge, and they have associated fronts that extend northward toward the cap (Figure 11). Interestingly, the associated front in Figure 11c has a wavy nature to it, with a wavelength of ~400 km, with additional spiral clouds trying to develop behind the main spiral cloud. The observed spiral clouds from late summer to early fall are well developed and larger in size (Figure 11). Condensate clouds are involved in these storms, and the storm development process resembles the baroclinic cyclogenesis on Earth (Figure 12).

5. South Polar Clouds

[37] As in the north, the south polar hood develops from a series of storms that first appear in late southern summer (Figure 13). By southern fall equinox, the south polar region is covered by circumpolar clouds. The south polar cap and hood grow northward from ~60°S to ~45°S during L_s 21° ~ 111°, and they retreat southward from ~45°S to ~60°S during L_s 134° ~ 197° (see Figure 2). This result suggests

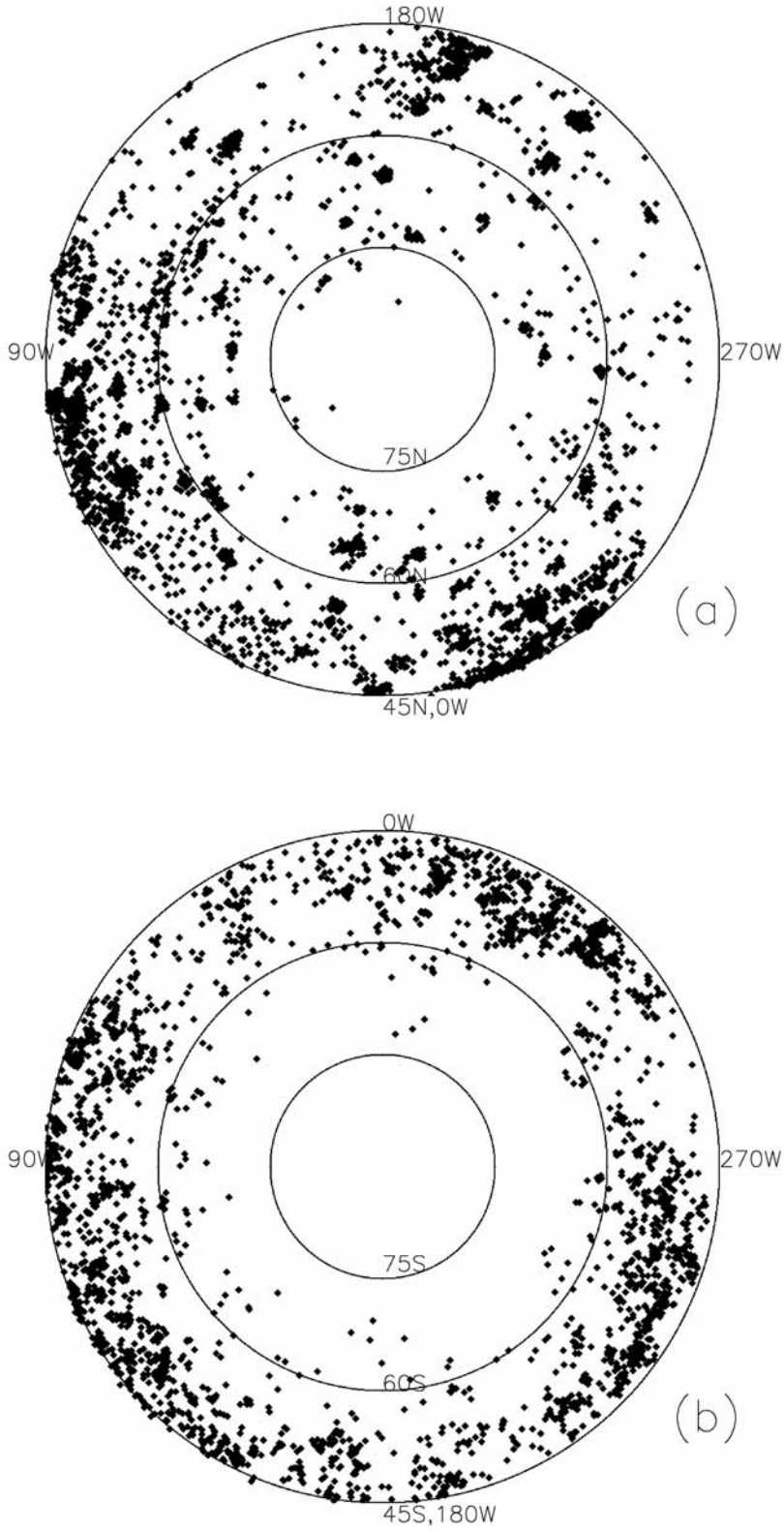

Figure 9. Spatial distribution of lee waves in the (a) north polar maps and (b) south polar maps. Each dot represents the position of an observed lee wave.

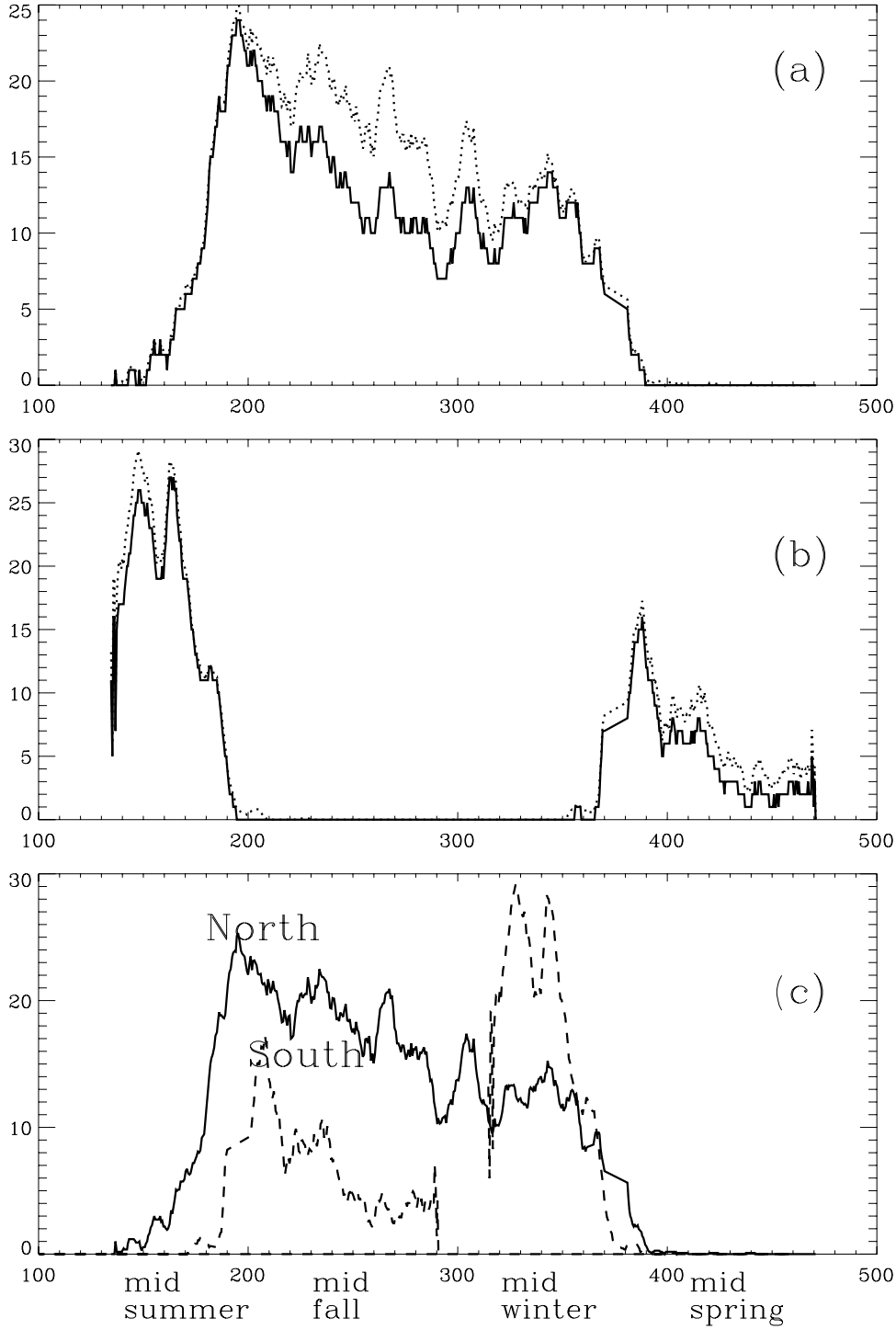

Figure 10. Temporal distribution of lee waves in the (a) north polar and (b) south polar maps The solid lines in Figures 10a and 10b are the number of lee waves observed in the polar maps as a function of L_s. The dotted lines in Figures 10a and 10b are from the solid lines scaled by the area outside the terminator circles. (c) The solid line is the scaled time sequence for the north polar region, the same as the dotted line in Figure 10a. The dashed line is the scaled time sequence for the south polar region with the L_s shifted by 180°.

faster retreat than growth in the latitudinal range from 45°S to 60°S.

5.1. Development of the South Polar Hood

[38] The south polar hood begins to develop around L_s ~340°. It evolves through two distinct stormy periods in late southern summer, and finally becomes circumpolar around the southern fall equinox (Figures 13g–13i). The development of the south polar hood is shown in Figure 14 as the fraction of cloud-covered area between 70°S and 80°S. The cloud-covered area is defined by the pixels in the red south polar map that are more than 75% brighter than the corre-

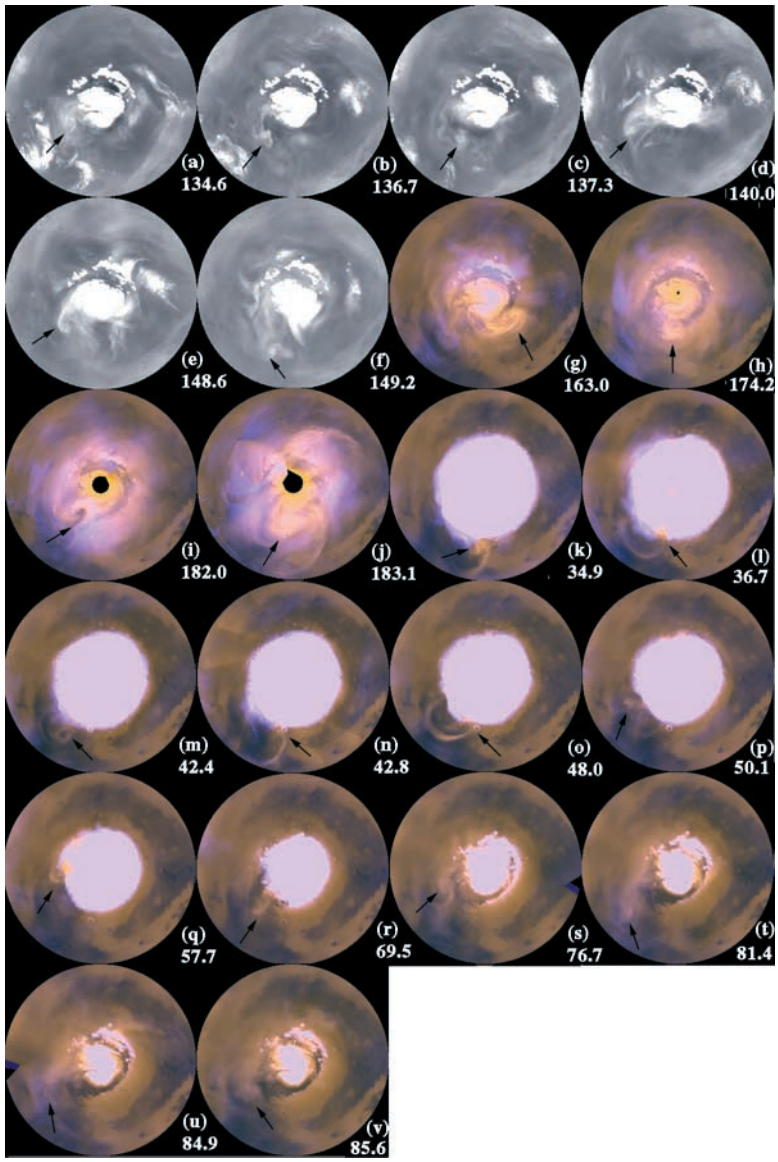

Figure 11. Spiral clouds observed by MOC during the observational period (L_s 134° ~ 360° ~ 111°). All the spiral clouds occur in the north polar region from mid spring to early fall. The panels are north polar stereographic maps (45°N-90°N, 0.1° × 0.1°) with the corresponding L_s shown below them.

sponding pixels in the reference red map. This criterion is different from the one used in the north, because different stretch was applied for the north and south polar maps. Both dust and condensate clouds can satisfy this criterion and are included in Figure 14. The first stormy period spans L_s 340° ~ 345° (Figures 13g and 14). The second stormy period starts from L_s ~352° (Figures 13h and 14), and becomes circumpolar around L_s ~0°. The cloud-covered area then decreases before additional dust storms occur in southern fall.

[39] The timing of these storms resembles the north polar hood development during the transitional period L_s 160° ~ 180°, where two regional dust storms precede the formation of the north polar hood. However, the southern dust storms are much smaller in size, and appear to involve few condensate clouds. Furthermore, none of the southern storms appear to display the characteristic fronts and spiral structures of the baroclinic storms seen in the north.

[40] Although the types of clouds in the winter are similar in the south polar region and the north polar region (compare Figure 6g with Figure 13a), clouds in the south polar region during the fall appear much thinner (compare Figures 6e and 6f with Figures 13j and 13k). Faint streak clouds surrounding the polar region can be seen in the south polar hood (Figures 13j–13l), but the number of streaks appears much less than that in the north polar region during the northern fall. Lack of water vapor in the southern hemisphere [*Jakosky and Farmer*, 1982] could contribute to this discrepancy.

5.2. South Polar Clouds From Midwinter to Midsummer

[41] The dominant clouds in the south polar hood change from streak clouds (Figure 13a) to haze and cap edge dust storms (Figure 13b) around southern spring equinox. *Cantor*

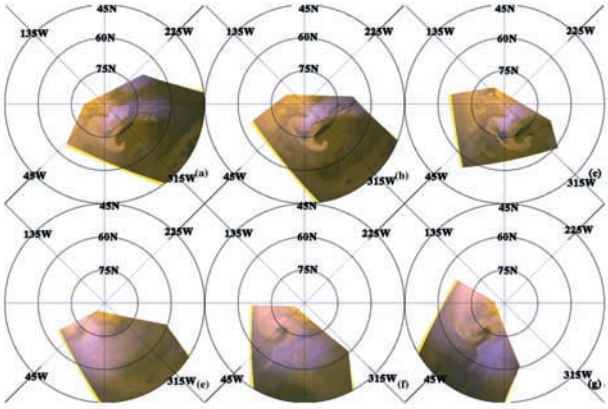

Figure 12. Spiral clouds in the north polar region during the transitional period (L_s 160° ~ 185°). Note the condensate clouds associated with the dust fronts. (a–c) Consecutive two-hour sequence at L_s ~163°. (e–g) Consecutive two-hour interval sequence at L_s ~182°.

et al. [2001] documented poleward recession of the cap edge dust storms before L_s ~274°. *Kahn* [1984] documented the same phenomenon for the Viking era. Before mid southern spring, the south polar cap recedes symmetrically [*James et al.*, 2001], and the local dust storms observed by MOC are evenly distributed around the polar cap [*Cantor et al.*, 2001]. However, after mid southern spring, the south polar cap recedes asymmetrically [*James et al.*, 2001], and the cap edge dust storms tend to occur in the 90°–180°–270°W sector (Figures 13d and 13e) [*Cantor et al.*, 2001]. A regional dust storm in the southern high latitudes observed by MOC during 1999 occurred at the beginning of the asymmetric recession phase around L_s ~234° [*Cantor et al.*, 2001]. These storms have settled by L_s ~274°.

[42] Clearer conditions (Figure 13f) after the southern summer solstice last until L_s ~340°. However, summer is not cloud-free. Individual global map swaths show that arc-shaped clouds often occur near the terminator (the 0200 LT side) during the summer (Figure 15). However, the early afternoon side (the 1400 LT side) is generally calm. Small dust storms occur only occasionally, and the exposed polar layered terrain appears to be a preferred area for them. The clouds near the terminator usually do not show clearly in the daily south polar map because the cloudy 0200 LT side of one image is merged with the 1400 LT side of another image (see sections 2 and 4.2).

5.3. South Polar Lee Waves

[43] Despite of the general lack of condensate clouds in the southern hemisphere, many lee waves are still observed in the south polar region. They preferably lie around the south polar cap during the fall and winter. Their spatial distribution is shown in Figure 9b. As in the north polar region, more lee waves are observed between 45°S and 60°S largely because of the lack of data within the terminator circles. The observed lee waves are roughly evenly distributed except in Hellas and Argyre. The lack of lee waves in these basins could be related to their relatively flat bottom topographies and compressional heating of the air. There are 2998 lee waves observed in the south polar region, and 4573 lee waves observed in the north polar region. The fact that more lee waves exist in the north polar region is consistent with more water vapor in the northern hemisphere [*Jakosky and Farmer*, 1982].

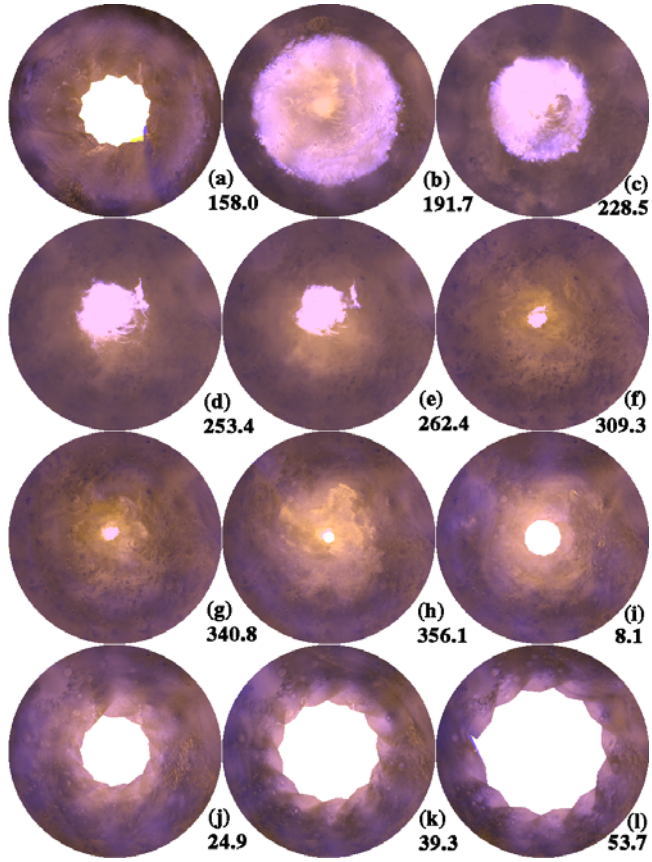

Figure 13. Representative south polar stereographic maps (45°S-90°S, 0.1° × 0.1°). L_s is indicated below each panel. The blank circular areas at the centers of the maps during the fall and winter are the areas inside the terminator circles. The polar cap in Figure 13a is larger than that in Figure 13b, but it appears darker because the stretches are different.

[44] The number of south polar lee waves as a function of L_s is shown in Figure 10b. To facilitate comparison in

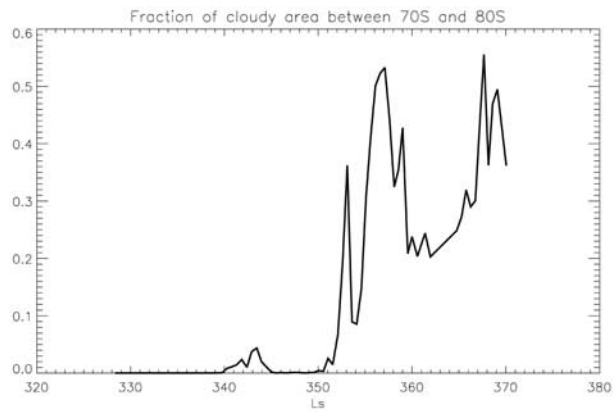

Figure 14. Fraction of cloud covered area within 70°S and 80°S as a function of L_s.

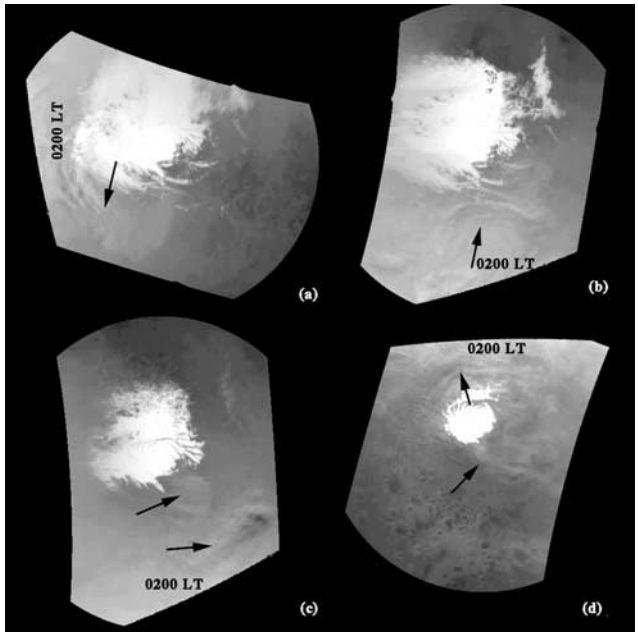

Figure 15. Dust activity in the south polar region in the southern summer. Each image is a stereographically projected red global map swath (65°S-90°S, 0.1° × 0.1°). Note the dust activity near the terminator (0200 LT). (a) From m10-00784 at L_s ~258°. (b) From m10-00892 at L_s ~259°. (c) From m11-00687 at L_s ~276°. (d) From m12-02041 at L_s ~304.5°.

Figure 10c, the scaled time sequence for the south polar region (the dotted line in Figure 10b) has been shifted by 180° L_s (the dashed line in Figure 10c) and overplotted with the original scaled time sequence for the north polar region (the solid line in Figure 10c). The number of south polar lee waves in the second Martian year suddenly increases around L_s ~5° and peaks around L_s ~30°. These events are about 15°–25° of L_s later in the season than their northern counterparts, and are consistent with the scarceness of water vapor in the south polar region. The number of south polar lee waves then decreases from mid southern fall to the end of our observational period L_s ~111°. Interestingly, the number of south polar lee waves in the first Martian year shows another set of sharp peaks around L_s ~150° and 160° respectively. These peaks are not only larger than the early fall peak in the south polar region, but they are also larger than the early fall peak in the north polar region. Due to the large extent of the seasonal south polar cap, some cap edge lee waves are observed at latitudes lower than 45°S in the equatorial maps, especially from mid fall to mid winter. These low latitude lee waves were not included in Figure 10. Further study is needed to see how they would influence the north-south difference shown in Figure 10c and to understand the global distribution of lee waves.

6. Conclusion

[45] In this study, we have processed MGS MOC global map swaths taken from May 1999 (L_s ~134°) to January 2001 (L_s ~111°). We have made Mars daily global maps from these data for the roughly one Martian year period and studied the cloud distribution. The maps show the evolution of the tropical cloud belt and the north and south polar hoods, and reveal the similarities and differences between the two polar hoods, including dust storms, streak clouds and lee waves. We describe a new type of "aster" cloud above the volcanoes, and we show the relation between the condensate and dust clouds in the spiral storms in the north polar region.

[46] The tropical cloud belt quickly disintegrates during L_s 134° ~ 149° of the first Martian year. Only the clouds associated with the volcanoes exist in the low latitudes during the northern fall and winter. The tropical cloud belt begins to develop around L_s ~44° of the second Martian year and becomes longitudinally continuous by L_s 57° ~ 70°. The cloud types change from convective clouds in mid northern summer to fibrous clouds in mid northern spring/early northern summer. The decaying phase and the developing phase of the cloud belt are nonuniform in longitude. The general behavior of the tropical cloud belt observed by MGS is similar to that derived for the Viking era [*Kahn*, 1984; *Tamppari et al.*, 2000], but differences in the developing and decaying phases exist.

[47] A new "aster" cloud pattern, consisting of rays around a central disk, is observed above the volcanoes in mid northern summer. Such clouds can be observed on all the main volcanoes, though they are best shown above Arsia Mons. Shadows indicate that rays are sometimes ~15 km or more above the surface. The time when such clouds are observed and the morphology of the clouds indicate that they form under weak atmospheric static stability and weak large-scale background flow, and they are probably related to the local upslope winds associated with the volcanoes.

[48] Following the observations by Viking and Hubble Space Telescope, MGS also observed spiral clouds. All the spiral clouds observed up to now occur in high northern latitudes from mid northern spring to early northern fall. The spiral clouds observed by MGS are different from the previous ones in that they are mainly composed of dust instead of water ice, and they sometimes have associated fronts or spiral arms. The dust clouds and condensate clouds occur in distinctly different parts of the spiral structure, supporting baroclinicity as the mechanism for the storm development. Baroclinic fronts and spiral clouds occur less frequently in the south, perhaps because the small residual south polar cap cannot supply enough cold air.

[49] Both the north polar hood and the south polar hood begin to develop in late summer about 20° L_s before the equinoxes. They both experience two stormy periods before the formation of the circumpolar clouds in early fall. However, there are significant differences between the two polar hoods. Condensate clouds appear common during the development of the north polar hood, but they seem rare during the development of the south polar hood. A wave number two stationary wave structure shows clearly in the north but not in the south. Perhaps because of the low abundance of water vapor in the south, streak clouds and lee wave clouds are less abundant in the south than in the north. In both polar regions, lee waves are observed mainly in the fall and winter, and the number of lee waves shows a peak in early fall. However, the temporal distributions for the northern and southern lee waves are quite different during this year. The south polar lee waves emerge about 15°–25°

L_s later than the north polar lee waves, and they show the largest peak in late winter.

[50] **Acknowledgments.** This work is supported by the Mars Global Surveyor project and by NASA grant number NAG5-11288. We would like to thank the USGS astrogeology team for providing us with an early version of the software for calculating the geometry backplanes. We thank Shawn Ewald for testing the code for mosiacing the daily global maps. We thank Arden Albee, Zhiming Kuang, and an anonymous referee for helpful comments and suggestions.

References

Barnes, J. R., J. B. Pollack, R. M. Haberle, C. B. Leovy, R. W. Zurek, H. Lee, and J. Schaeffer, Mars atmospheric dynamics as simulated by the NASA Ames general circulation model, 2, Transient baroclinic eddies, *J. Geophys. Res.*, *98*, 3125–3148, 1993.

Barnes, J. R., R. M. Haberle, J. B. Pollack, H. Lee, and J. Schaeffer, Mars atmospheric dynamics as simulated by the NASA Ames general circulation model, 3, Winter quasi-stationary eddies, *J. Geophys. Res.*, *101*, 12,753–12,776, 1996.

Cantor, B. A., P. B. James, M. Caplinger, and M. J. Wolff, Martian dust storms: 1999 Mars Orbiter Camera observations, *J. Geophys. Res.*, *106*, 23,653–23,687, 2001.

Caplinger, M., Mars Observer Camera MOC2 calibration report, MSSS internal document, version 1.3, San Diego, Calif., Oct. 1997.

French, R., P. Gierasch, B. Popp, and R. Yerdon, Global patterns in cloud forms on Mars, *Icarus*, *45*, 468–493, 1981.

Gierasch, P., P. Thomas, R. French, and J. Veverka, Spiral clouds on Mars: A new atmospheric phenomenon, *Geophys. Res. Lett.*, *6*, 405–408, 1979.

Haberle, R. M., J. B. Pollack, J. R. Barnes, R. W. Zurek, C. B. Leovy, J. R. Murphy, H. Lee, and J. Schaeffer, Mars atmospheric dynamics as simulated by the NASA Ames general circulation model, 1, The zonal mean circulation, *J. Geophys. Res.*, *98*, 3093–3123, 1993.

Hapke, B., Bidirectional reflectance spectroscopy, 4, Extinction and the opposition effect, *Icarus*, *67*, 264–280, 1986.

Hollingsworth, J. L., R. M. Haberle, J. R. Barns, A. F. C. Bridger, J. B. Pollack, H. Lee, and J. Schaeffer, Orographic control of storm zones on Mars, *Nature*, *380*, 413–416, 1996.

Houze, R. A. Jr., *Cloud Dynamics*, 573 pp., Academic, San Diego, Calif., 1993.

Hunt, G. E., and P. B. James, Martian extratropical cyclones, *Nature*, *278*, 531–532, 1979.

Jakosky, B. M., and C. B. Farmer, The seasonal and global behavior of water vapor in the Mars atmosphere—Complete global results of the Viking atmospheric water detector experiment, *J. Geophys. Res.*, *87*, 2999–3019, 1982.

James, P. B., Martian local dust storms, in *Recent Advances in Planetary Meteorology*, edited by G. Hunt, pp. 85–100, Cambridge Univ. Press, New York, 1985.

James, P. B., and B. A. Cantor, Martian north polar cap recession: 2000 Mars Orbiter Camera observations, *Icarus*, *154*, 131–144, 2001.

James, P. B., J. F. Bell, R. T. Clancy, S. W. Lee, L. J. Martin, and M. J. Wolff, Global imaging of Mars by Hubble space telescope during the 1995 opposition, *J. Geophys. Res.*, *101*, 18,883–18,890, 1996.

James, P. B., J. L. Hollingsworth, M. J. Wolff, and S. W. Lee, North polar dust storms in early spring on Mars, *Icarus*, *138*, 64–73, 1999.

James, P. B., B. A. Cantor, and S. Davis, Mars Observer Camera observations of the Martian south polar cap in 1999–2000, *J. Geophys. Res.*, *106*, 23,635–23,652, 2001.

Kahn, R., The spatial and seasonal distribution of Martian clouds and some meteorological implications, *J. Geophys. Res.*, *89*, 6671–6688, 1984.

Leovy, C. B., G. Briggs, A. Young, B. Smith, J. Pollack, E. Shipley, and R. Widley, The Martian atmosphere: Mariner 9 television experiment progress report, *Icarus*, *17*, 373–393, 1972.

Malin, M. C., and K. S. Edgett, The Mars Global Surveyor Mars Orbiter Camera: Interplanetary Cruise through Primary Mission, *J. Geophys. Res.*, *106*, 23,429–23,570, 2001.

Martin, L. J., P. B. James, A. Dollfus, and K. Iwasaki, Telescopic observations: Visual, photographic, polarimetric, in *Mars*, edited by H. H. Kieffer et al., pp. 34–70, Univ. of Ariz. Press, Tucson, 1992.

Pettengill, G. H., and P. G. Ford, Winter clouds over the north Martian polar cap, *Geophys. Res. Lett.*, *27*, 609–612, 2000.

Richardson, M. I., R. J. Wilson, and A. V. Rodin, Water ice clouds in the Martian atmosphere: General circulation model experiments with a simple cloud scheme, *J. Geophys. Res.*, *107*, 10.1029/2001JE001804, in press, 2002.

Rodin, A. V., R. T. Clancy, and R. J. Wilson, Dynamical properties of Mars water ice clouds and their interactions with atmospheric dust and radiation, *Adv. Space. Res.*, *23*, 1577–1585, 1999.

Smith, A. D., J. C. Pearl, B. J. Conrath, and P. R. Christensen, Thermal Emission Spectrometer results: Mars atmospheric thermal structure and aerosol distribution, *J. Geophys. Res.*, *106*, 23,929–23,945, 2001.

Snyder, C. W., The mission of the Viking Orbiters, *J. Geophys. Res.*, *82*, 3971–3983, 1977.

Snyder, C. W., and V. I. Moroz, Spacecraft exploration of Mars, in *Mars*, edited by H. H. Kieffer, pp. 71–119, Univ. of Ariz. Press, Tucson, 1992.

Tamppari, L. K., R. W. Zurek, and D. A. Paige, Viking era water-ice clouds, *J. Geophys. Res.*, *105*, 4087–4107, 2000.

A. P. Ingersoll and H. Wang, Division of Geological and Planetary Sciences, California Institute of Technology, MS 150-21, Pasadena, CA 91125, USA. (hqw@gps.caltech.edu)